Int. J. Heat Mass Transfer. Vol. 26, No. 7, pp. 993-1005, 1983
Printed in Great Britain

0017-9310/83 $3.00 + 0.00

EFFECT OF INTERWALL SPACING AND FLUID FLOW INLET CONDITIONS ON A CORRUGATED-WALL HEAT EXCHANGER

E. M. SPARROW and J. W. COMB
Department of Mechanical Engineering, University of Minnesota, Minneapolis, MN 55455, U.S.A.

(*Received* 4 *October* 1982 *and in revised form* 17 *November* 1982)

Abstract—Heat transfer, pressure drop, and patterns of fluid flow were determined experimentally for water flowing in a corrugated-wall duct. Consideration was given to the effects of varying the spacing between the corrugated walls and of different fluid flow inlet conditions; the role of the noncorrugated side walls in the evaluation of the heat transfer coefficient was also examined. The increase of the interwall spacing gave rise to a substantial increase in the fully developed Nusselt number (30% for the investigated spacing variation), but the friction factor increased to a greater extent (more than a factor of two). Performance evaluations were carried out for three different constraints—fixed pumping power, fixed pressure drop, and fixed mass flow. For all of these cases, the heat transfer coefficient for the larger interwall spacing was slightly lower than that for the smaller interwall spacing, but the pressure drop was also lower. Fluid inlet configurations were employed which created different degrees of turning of the flow. It was found that the greater the turning, the higher the entrance region heat transfer coefficients.

NOMENCLATURE

A_{sw}, side-wall area;
A_w, corrugated-wall area;
c_p, specific heat;
D_h, hydraulic diameter;
f, friction factor, equation (7);
H, interwall spacing, Fig. 1;
h, cycle-average fully developed heat transfer coefficient, equation (2);
k, thermal conductivity;
$\dot{m}$, mass flow rate;
Nu, cycle-average fully developed Nusselt number, hD_h/k;
P, perimeter;
PP, pumping power;
Pr, Prandtl number;
p_{atm}, pressure in laboratory;
p, local pressure at X;
Q_{cycle}, heat added to fluid per cycle;
Re, Reynolds number, $4\dot{m}/\mu P$;
S, axial length of a cycle;
T_b, fluid bulk temperature;
T_{sw}, side-wall temperature;
T_w, corrugated-wall temperature;
V, mean velocity;
W, spanwise width of duct;
X, axial coordinate;
X', shifted X coordinate.

Greek symbols

η, weight function for side-wall area;
θ_{sw}, dimensionless side-wall temperature, $(T_{sw}-T_b)/(T_w-T_b)$;
ρ, density;
μ, viscosity.

Subscripts

fd, fully developed;
x, at location X;
1, configuration of ref. [1].

INTRODUCTION

IN A PREVIOUS paper [1], definitive heat transfer data were obtained for water flow in a corrugated-wall duct. The heat transfer results were supplemented by pressure drop measurements and by flow visualization studies. The present investigation constitutes a continuation of the earlier work [1], with a considerable enlargement of scope. There are three main foci of the experimental work to be performed here, as will now be described.

To motivate the first phase of the work, it should be noted that although the results of ref. [1] were presented in dimensionless form (Nusselt, Reynolds, and Prandtl numbers), their generality with respect to changes in duct dimensions remains uncertain. The issue of particular concern here is the spacing between the corrugated walls. There are reasons to expect that the pattern of fluid flow over the corrugation facets will change as the interwall spacing is varied, specifically, the extent to which the forward- and rearward-facing facets are washed by separated, recirculating fluid. The change of flow pattern with changes in duct dimensions is a special feature of the complex corrugated-duct geometry that is not encountered in conventional ducts such as circular and annular tubes and rectangular ducts.

Heat transfer and pressure drop measurements, supplemented by flow visualization, will be performed for a duct of greater interwall spacing than that of ref. [1]. Although a dimensionless correlation of the heat transfer results will be presented, more incisive comparisons with ref. [1] are made in terms of the heat transfer coefficient itself rather than in terms of the Nusselt number. Specific comparisons are made for the constraints of equal mass flow, equal pressure drop, and equal pumping power.

The second focus of the work concerns the way in which the fluid enters the duct. In practical heat exchange devices, plenum chambers or headers of

various configurations may be employed to feed a parallel array of ducts whose inlets are built into one of the walls of the plenum (e.g. a tube sheet). If fluid is supplied to the upstream end of the plenum and if the plenum is relatively short, then the fluid particles will have to move along curved paths to reach certain of the duct inlets. Similarly, fluid supplied to the plenum via a port in the side of the plenum will also move along trajectories that are highly curved. Another complex inlet flow will be encountered if the duct, instead of being linear from end to end, is folded back on itself one or more times.

The fluid inlet configuration employed earlier [1] corresponded to the ideal condition in which the duct inlet faced upstream into a large plenum equipped with screens and a baffle plate. These design features provided a uniform inlet flow with a minimum of disturbances. For the present experiments, a configuration was employed which gave rise to a highly complex inlet flow. As will be described diagrammatically shortly, the fluid was delivered to the inlet in such a manner as to impart to it a velocity perpendicular to the linear axis of the corrugated duct. This required that the fluid turn sharply as it entered the duct. Furthermore, since the facets of a corrugated duct are sloping, two different inlet-flow delivery configurations were employed to provide both acute-angle and obtuse-angle turning.

The third focus of the work dealt with the role of the non-corrugated side walls of the duct in the heat transfer process. Both the duct employed here and that of ref. [1] were of fairly high cross-sectional aspect ratio, respectively 6.9 and 10. Consequently, the heat transfer surface area of the side walls was substantially smaller than that of the corrugated walls, but not negligible as implied by the data reduction scheme of ref. [1]. The side walls were not directly heated but received heat by conduction from the electrically heated corrugated walls. Three data-reduction models were employed to assess the effect of the side-wall heat transfer on the duct Nusselt number, including a re-examination of the data of ref. [1].

The heat transfer experiments performed here were carried out using water as the working fluid and spanned the Reynolds number range from 2000 to 27000. For these experiments, the Prandtl number ranged from 4 to 12. The fluid flow experiments were performed without heat transfer in a separate apparatus using air. Pressure drop measurements were made to yield friction factors, and duplicate data using alternate instrumentation were obtained to ensure the reliability of the results. The oil–lampblack technique was used for the flow visualization.

The relevant literature on corrugated-duct heat transfer has already been cited [1].

EXPERIMENTAL APPARATUS

As noted earlier, separate water-flow and airflow apparatuses were employed during the course of the investigation, respectively for the heat transfer and fluid flow studies. The water-flow system will be described first, followed by the airflow system. To attain a more compact description, certain apparatus details will be omitted since they may be found in ref. [1].

Apparatus for heat transfer experiments

The water-flow system was operated in the open-circuit mode, supplied at its upstream end with water from an elevated constant head tank and discharging the water to a drain at the downstream end. The constant head tank received adjustable amounts of hot and cold water from the building lines, the hot–cold balance being selected to obtain the desired Prandtl number. From the head tank, the water passed downward through a pipeline, which delivered it to the entrance port of a large plenum chamber. The plenum was equipped with a baffle plate and screens designed to provide a uniform, disturbance-free flow to the test section inlet which was built into the downstream wall of the plenum. After traversing the test section, the water exited into a plenum, from which it was ducted through a riser, to a weight tank, and then to the drain.

The geometry of the corrugated-wall passage investigated here is shown in a side-view schematic in Fig. 1, which also conveys a comparison with that of ref. [1]. As seen there, each corrugated wall consists of a succession of forward-facing and rearward-facing facets, with the corrugations of the two walls being in phase. The geometry of the passage is periodic, and S is used to denote the axial length of one cycle. It should also be noted that the peaks and valleys are sharp-edged (i.e. not rounded).

Three quantities have to be specified to define the passage geometry. These include the interwall spacing H (measured perpendicular to the walls), the cycle length S, and the slope of the corrugation facets. For the present geometry, $H = 0.737$ cm, $S = 2.032$ cm, and the slope angle = 30°. The overall length of the channel included 10 corrugation cycles (20 facets per wall). The spanwise dimension of the channel was 5.08 cm, yielding a cross-sectional aspect ratio of 6.9.

The channel used in ref. [1] is defined by the interwall spacing $H_1 = 0.508$ cm, where a dashed line has been employed in the figure to indicate the position of the upper wall of the channel. The increase in the present interwall spacing relative to that of ref. [1] was intended to represent a significant change, but not one that would be so large as to lose the character of the corrugated channel. For large interwall spacings, the

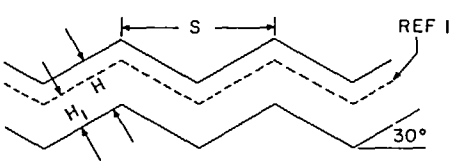

FIG. 1. Geometry of the corrugated-wall duct and comparison with that of ref. [1].

passage would become a rough-walled rectangular duct rather than a corrugated-wall channel.

The various fluid flow inlet conditions employed during the course of the investigation will now be discussed, and Fig. 2 has been prepared in this connection. Figures 2(a)–(c) each illustrate one of the inlet configurations. Each shows a portion of the downstream wall of the plenum chamber, the inlet of the corrugated duct, and the first few corrugation cycles. The plenum chamber extends to the left of the wall, and it provides a uniform approach flow at stations sufficiently upstream of the inlet, as illustrated at the left of Fig. 2(a).

Figure 2(c) shows the inlet configuration that was employed both in ref. [1] and in the initial phase of the present investigation. In that case, the inlet opens freely onto the plenum, without obstruction. In the other two configurations, a delivery duct is employed which forces the water to flow parallel to the downstream wall of the plenum before it encounters the inlet of the corrugated passage. This arrangement requires that the fluid execute a sharp turn as it passes from the delivery duct to the corrugated passage. The cross-sectional dimensions of the delivery duct were chosen to closely approximate those of the passage.

In Fig. 2(a), the delivery duct is positioned so that its entrance is at the bottom. Therefore, since the first portion of the corrugated passage is downsloping, the flow entering the passage from the delivery duct must turn by more than 90°. Figure 2(b) shows the delivery duct with its entrance at the top, and in this case the fluid flowing from the delivery duct into the passage turns by less than 90°.

As indicated in Fig. 2, the apparatus was designed so that the forwardmost faces of the corrugated duct did not contact the water in the plenum. Such contact would have given rise to substantial extraneous heat losses. Furthermore, for the same reason, the design also avoided contact between the forwardmost faces and the metallic wall of the plenum.

The desired minimization of heat losses was accomplished by use of a thin sheet of fiberglass circuit-board (0.12 cm thick) to replace the metallic wall of the plenum in the zone surrounding the inlet of the corrugated passage. The fiberglass board, which has a very much lower thermal conductivity than the metallic wall, served as a barrier between the forwardmost faces of the corrugated passage and the water in the plenum. As a further defense against extraneous losses, the front ends of the corrugated walls were beveled to minimize the contact area with the thermal barrier. Silicone rubber was used to seal the contact.

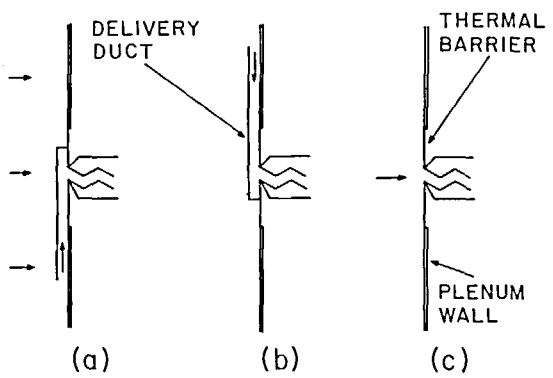

FIG. 2. Fluid flow inlet configurations.

The corrugated walls were each fabricated from 1.27 cm thick copper plate. The corrugation facets were made utilizing a V-shaped tool with a 120° included angle in conjunction with a horizontal milling machine. Each of the side walls was also of copper, 0.508 cm thick, into which a longitudinal groove was milled to accommodate an O-ring. For the assembly of the duct, the side walls were pressed tightly against the side edges of the corrugated walls by clamps.

Heating was accomplished by electrical resistance wire embedded in closely spaced spanwise grooves that had been milled into the rear face of each of the corrugated walls. The temperature of each facet was measured by a thermocouple positioned at the spanwise and streamwise midpoints of the facet, with the thermocouple junction situated within 0.0254 cm of the sloping surface. These thermocouples were placed in holes drilled from the rear face of the duct. Side-wall temperatures were measured at the 9th, 10th, and 11th facets, these locations having been chosen because they fall in the thermally developed regime. Each side-wall thermocouple was positioned at the streamwise midpoint of its facet, and it was also centered in the channel height, midway between the upper and lower corrugated walls.

All thermocouples were made from 0.0127 cm diameter Teflon-coated copper and constantan wire that had been specifically calibrated for the present experiments. The thermocouples were read with a programmable 1 μV datalogger.

Apparatus for fluid flow experiments

The airflow apparatus was used for both pressure drop measurements and flow visualization and, in deference to the latter, the apparatus was made of Plexiglas. With the available measurement techniques, definitive pressure drop information could be obtained only for the hydrodynamically developed regime. Consequently, the fluid flow inlet conditions are not an issue, and the experiments were performed with the unobstructed inlet pictured in Fig. 2(c). For convenience, the apparatus was operated in the suction mode, with the laboratory room serving as the upstream plenum. Air was drawn into the inlet by a blower positioned aft of the downstream plenum chamber.

The corrugated duct of the airflow apparatus was made with the same internal dimensions (i.e. interwall spacing, facet angle, cycle length, number of cycles, and spanwise width) as the corrugated duct of the heat transfer apparatus. A pressure tap was installed in each of the facets, positioned at the spanwise and streamwise

midpoints. The taps were connected by plastic tubing to a specially fabricated pressure selector switch having a single output.

Preliminary measurements yielded remarkably high values of the friction factor (in excess of one). In order to establish the validity of the results, data duplication was sought by employing various measurement instruments. For pressure, the primary instrument was a Baratron solid-state, capacitance-type pressure meter. Two different Baratron sensing heads were used, one with an upper limit of 10 Torr and the other with an upper limit of 100 Torr, the former for the lower Reynolds numbers and the latter for the higher Reynolds numbers. In the mid-range, both heads were used for verification purposes. Also, at the higher Reynolds numbers, the pressure drops were large enough to permit the use of a manometer, thereby providing another independent check.

For the airflow measurement, two calibrated rotameters were used, respectively for the lower and higher flow-rate ranges, but with a range of overlap for checking purposes. An additional independent verification was obtained by means of a calibrated orifice.

The flow visualization was accomplished by the use of the oil–lampblack technique. With this technique, a mixture of lampblack powder and oil is brushed on the surface which bounds the airflow. Ideally, under the action of the forces exerted by the flow, the mixture will move along the surface, following the paths of the fluid particles which pass adjacent to the surface. In regions of low velocity (e.g. reattachment zones), the mixture will remain stationary, so that such regions show themselves as black, streak-free zones on the surface.

To obtain a permanent record of the visualized flow pattern, white, plasticized, self-adhering contact paper was affixed to the corrugations of the lower wall of the duct and the oil–lampblack mixture applied to the contact paper. Once the visualization pattern had been formed, the contact paper was carefully separated from the duct wall and laid flat on a sheet of cardboard for photography.

DATA REDUCTION

The main focus of the heat transfer experiments was the determination of fully developed heat transfer coefficients and Nusselt numbers, although the thermal entrance region was also explored in connection with the various fluid flow inlet conditions. With regard to the fully developed regime, it is, in principle, independent of the flow inlet condition, and this property was verified by the actual experimental data.

In a duct characterized by geometric periodicity, as that investigated here, the thermally developed regime is distinctly different from that for conventional ducts of axially unchanging cross section. For conventional ducts, thermal development is characterized by a heat transfer coefficient that is the same at all axial stations. For a duct of periodic geometry, the heat transfer coefficient may vary axially in the thermally developed regime, but the same value of the coefficient recurs periodically at successive axial stations separated by a distance S. In addition, the cycle-average heat transfer coefficient is the same from cycle to cycle. For ducts with periodic geometry, it is common to employ the designation *periodic* fully developed regime.

For the uniform heating condition employed in the present experiments, the wall temperatures T_w at axial positions X_1, (X_1+S), (X_1+2S), (X_1+3S),... in the fully developed region should lie on a straight line (X_1 is arbitrary). Furthermore, the fluid bulk temperatures at the same set of points should lie on a parallel straight line. The slope of these straight lines is

$$dT/dX = Q_{cycle}/S\dot{m}c_p \tag{1}$$

where Q_{cycle} is the heat added to the fluid in each cycle. Also, in the fully developed regime, the axial conduction in the duct wall at X_1 has to be equal to that at (X_1+S), (X_1+2S),..., that is, the *net* axial conduction is zero. Therefore, in the present experiments, Q_{cycle} is equal to the electrical power supplied by the embedded heating wires to the duct in each cycle.

Cycle-average fully developed heat transfer coefficients were evaluated from the measured temperatures and heat inputs. The wall-to-bulk temperature difference needed for the evaluation was determined by employing the principles discussed in the preceding paragraph. The bulk temperature was represented by a straight line having a slope given by equation (1) and passing through the measured inlet value $T_b = T_{bi}$ at the onset of heating. A straight line of the same slope was passed through the measured facet wall temperatures in the fully developed regime. By intent, the measurement locations at successive, correspondingly sloped facets were separated by the cycle length S. The vertical displacement of the wall temperature line from the bulk temperature line yielded (T_w-T_b) for the fully developed regime.

Then, with Q_{cycle} and $(T_w-T_b)_{fd}$, the cycle-average heat transfer coefficient was found from

$$h = Q_{cycle}/(T_w-T_b)_{fd}\{A_w+\eta A_{sw}\}_{cycle}. \tag{2}$$

In this expression, A_w is the surface area of the facets, and A_{sw} is the surface area of the side walls, both per cycle. The factor η ($\leqslant 1$) is inserted to weight the side-wall area, that is, to take account of the possibility that the side walls are at a lower temperature than that of the corrugation facets. Three models were used for η. Two were the limits $\eta = 1$ and $\eta = 0$. The other was based on the measured side-wall temperature T_{sw}

$$\eta = (T_{sw}-T_b)/(T_w-T_b) = \theta_{sw} \tag{3}$$

where T_{sw}, T_w, and T_b all correspond to the same axial station. These choices of η will be elaborated later. For the present duct configuration, $A_{sw}/A_w = 0.145$, while for the duct of ref. [1], $A_{sw}/A_w = 0.1$.

A dimensionless presentation was achieved by the use of the Nusselt, Reynolds, and Prandtl numbers

$$Nu = hD_h/k, \quad Re = 4\dot{m}/\mu P, \quad Pr = c_p\mu/k \tag{4}$$

where all fluid properties were evaluated at the mean bulk temperature (the overall rise in bulk temperature was about 1°F). If W denotes the spanwise width of the flow passage, then $D_h = 4HW/P$ and $P = 2(H+W)$.

The results were correlated in the form

$$Nu = CRe^m Pr^n. \tag{5}$$

The correlation was obtained by first selecting a likely value for the exponent n and writing $Nu/Pr^n = CRe^m$. The numerical values of Nu/Pr^n from the experimental data were used as input to this equation, and the quantities C and m were found from a least-squares fit. Then, for the next step, the thus-determined m value was employed to evaluate Nu/Re^m for each data point, and with $Nu/Re^m = CPr^n$, C and n were obtained via least squares. Next, with this n, Nu/Pr^n was calculated for each data point, and C and m were found from a least-squares fit of $Nu/Pr^n = CRe^m$. This process was continued until m, n, and C became invariant.

For the thermal entrance region, representative results will be reported in terms of the ratio

$$(T_w - T_b)_x/(T_w - T_b)_{fd}. \tag{6}$$

The numerator of this ratio corresponds to the wall-to-bulk temperature difference at an axial station X, while the denominator is the fully developed value. The departure of the ratio from unity reflects the deviation of the heat transfer coefficient at X from the fully developed coefficient.

Turning next to the friction factor, it may be noted that for periodically fully developed flow, the pressures at points $X_1, (X_1+S), (X_1+2S), \ldots$ lie on a straight line. For each measured pressure distribution, dp/dX was evaluated via least squares. With this, f was determined from

$$f = -(dp/dX)D_h/\tfrac{1}{2}\rho V^2 \tag{7}$$

with

$$V = \dot{m}/\rho(HW).$$

FLOW VISUALIZATION RESULTS

Representative photographs of the oil-lampblack flow visualization patterns are presented in Fig. 3. As noted earlier, white, plasticized contact paper, affixed to the lower-wall corrugations during a visualization run, was detached after the run and laid flat for photography, as in Fig. 3.

The upper photograph of Fig. 3 is a view looking down on a complete corrugation cycle, which, in the flow direction (indicated by the arrow), includes a peak, a rear-facing facet, a valley, a front-facing facet, and another peak. The photograph contains streaks and black bands which reveal the pattern of fluid flow adjacent to the surfaces of the respective facets.

The streaks which are in evidence on the entire rear-facing facet depict the tracks of a backflow, that is, a flow that is moving opposite to the mainstream direction. Furthermore, a portion of the front-facing facet is also washed by the backflow. This region extends forward from the valley of the corrugation to the black band which corresponds to the location at which the mainflow (i.e. the forward flow) reattaches to the surface. The remainder of the front-facing facet is washed by a forward flow.

The aforementioned backflow is indicative of flow separation which occurs at a corrugation peak because the fluid is unable to turn sufficiently sharply to follow

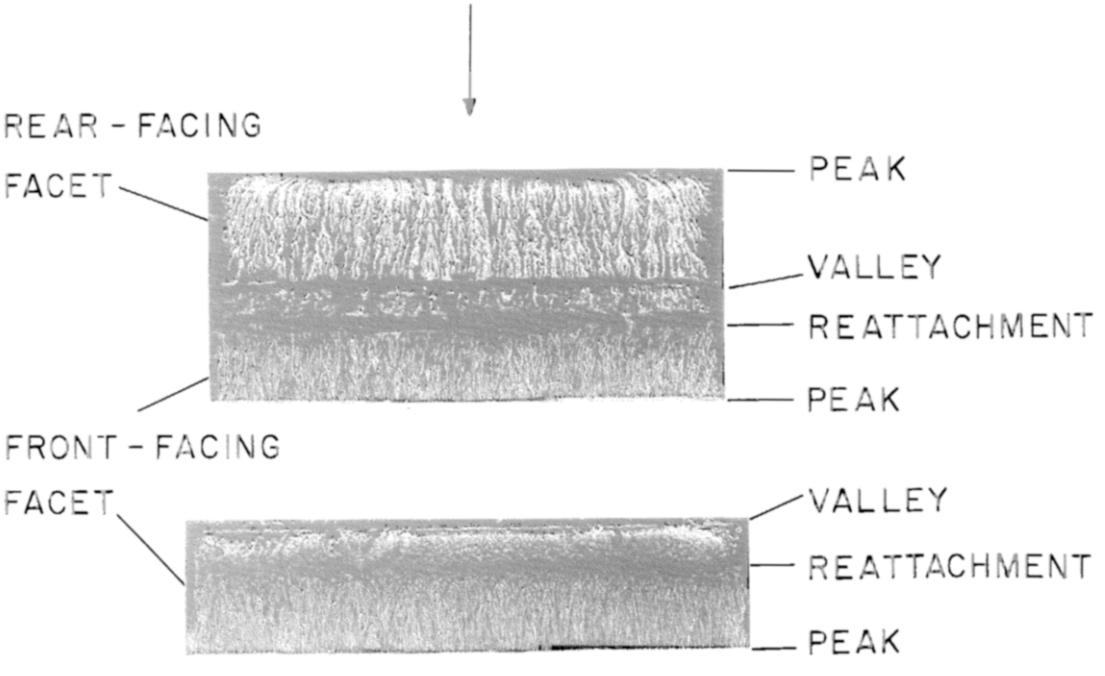

FIG. 3. Flow visualization patterns.

the surface contour. The backflow is the surface-adjacent leg of a pocket of recirculating fluid. Since the backflow extends over the entire rear-facing facet and over about one-third of the front-facing facet, more than half the surface area of each corrugation cycle is blanketed by the recirculation zone. It is also interesting to note the curvature of the streaklines in the backflow region which indicates the presence of spanwise motions, especially near the side walls, so that the flow is three-dimensional.

To obtain a sharper portrayal of the reattachment line, the fluidity of the oil–lampblack mixture was altered, yielding the photograph of the front-facing facet that is shown in the lower portion of Fig. 3. The reattachment line is seen to be straight, and the forward-flow downstream of the reattachment appears to be basically two-dimensional.

The visualization results of Fig. 3 will now be compared with those of ref. [1]. The main difference between the flow patterns is that for the smaller interwall spacing of ref. [1], the entire front-facing facet was washed by a forward flow, and the backflow was confined to the rear-facing facet. Thus, the increase in the interwall spacing has increased the size of the region of separated, recirculating flow. Since separated regions have different heat transfer characteristics than do forward-flow regions, differences between the present heat transfer results and those of ref. [1] can be expected. Another factor which may contribute to such differences is that the backflow observed in ref. [1] appeared to be more two-dimensional than that encountered here.

HEAT TRANSFER RESULTS

The presentation of results will begin with the fully developed heat transfer coefficients and Nusselt numbers, which are common to all the investigated fluid flow inlet conditions. The effect of the inlet conditions will then be examined via a presentation of local wall-to-bulk temperature differences in the entrance region.

Fully-developed Nusselt numbers

As was noted in the data reduction section, the evaluation of the fully developed heat transfer coefficient from equation (2) involves the selection of the factor η which weights the area A_{sw} of the side walls. It is, therefore, relevant to discuss the thermal conditions at the side walls.

The side walls are not externally heated, but receive their heat by conductive contact with the edges of the corrugated walls. Therefore, the side walls behave like fins which bridge between the heated corrugated walls. Since each side-wall thermocouple was positioned midway between the two corrugated walls, it measured the lowest side-wall temperature at the axial station at which it was installed.

The experimentally determined side-wall temperatures are presented in Fig. 4. On the ordinate, the difference between the side-wall and bulk temperatures is compared with the difference between the corrugated-wall and bulk temperatures, all at the same axial station. This ratio is plotted as a function of the Reynolds number, with the Prandtl number appearing as a parameter for the data. The figure shows that the side-wall temperature drops more and more below the corrugated-wall temperature as the Reynolds number increases, which is consistent with the fin-like nature of the side wall. The plotted ratio depends weakly on the Prandtl number, if at all. A least-squares fit of the data yields

$$\theta_{sw} = (T_{sw} - T_b)/(T_w - T_b) = 3.10\,Re^{-0.165}. \quad (8)$$

Fully developed heat transfer coefficients were evaluated from equation (2) employing $\eta = \theta_{sw}$ as well as the limits $\eta = 0$ and $\eta = 1$. To illustrate the lay of the experimental data with respect to its correlating line, the Nusselt number results based on $\eta = \theta_{sw}$ are plotted in Fig. 5. As seen in the figure, the overall range of the Reynolds number extends from about 2000 to 27 000. The Prandtl number, which serves as a parameter for the data points, extends from 4 to 12.

A least-squares correlation of the data yields

$$Nu = 0.386\,Re^{0.648}\,Pr^{0.3}, \quad (\eta = \theta_{sw}). \quad (9)$$

This equation is plotted in Fig. 5, where it is seen that there is only very slight data scatter relative to the line. The 0.648 exponent on the Reynolds number is reminiscent of that for separated flows ($\sim 2/3$) and is in the range of that for tube banks in crossflow. Both the present corrugated duct and the tube bank include significant zones of flow separation. The 0.3 exponent on the Prandtl number is very slightly lower than literature values for duct flows, and this may reflect the dominant role of the flow separation.

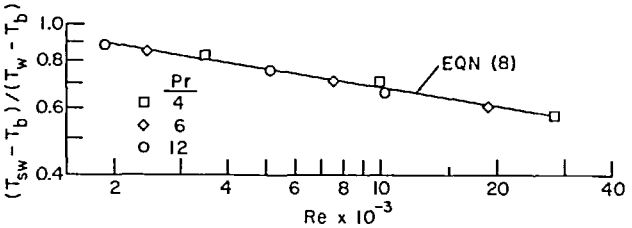

FIG. 4. Measured side-wall temperatures.

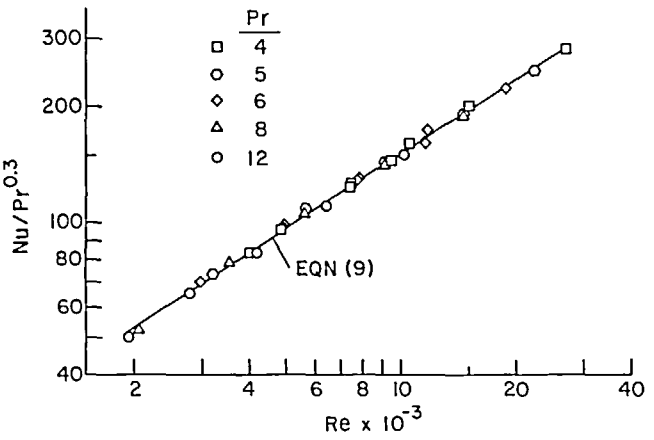

FIG. 5. Fully developed Nusselt numbers based on $\eta = \theta_{sw}$ as the weight for the side-wall area.

The Nusselt number results for each of the three choices of η, namely, $\eta = 0$, θ_{sw}, and 1 are brought together in Fig. 6. To avoid overlap and confusion, the data symbols have been omitted and only the least-squares lines are shown. (The extent of the data scatter is similar to that of Fig. 5.) The equations for the $\eta = 0$ and $\eta = 1$ lines are

$$Nu = 0.491\, Re^{0.632}\, Pr^{0.3}, \quad (\eta = 0), \tag{10}$$

$$Nu = 0.429\, Re^{0.632}\, Pr^{0.3}, \quad (\eta = 1). \tag{11}$$

Since $\eta = 0$ and $\eta = 1$ are constants, they yield correlations with the same power of the Reynolds number. However, since θ_{sw} is a function of the Reynolds number, correlation (9) has a different Reynolds number dependence than equations (10) and (11).

As seen in the figure, the line for $\eta = 0$ lies highest, that for $\eta = \theta_{sw}$ is intermediate, while that for $\eta = 1$ is the lowest. This ordering is plausible when the meanings of the various η models are examined. The $\eta = 0$ model does not include any of the side-wall area in the participating heat transfer surface area and, therefore, yields values of the Nusselt number that are too high. On the other hand, the $\eta = 1$ model assumes that the side-wall temperature is equal to the temperature of the corrugated walls and, thereby, weights the side-wall area equally with the corrugated-wall area. This procedure weights the side-wall area too heavily, since $(T_{sw} - T_b)/(T_w - T_b) \leqslant 1$, and leads to too-low Nusselt number values.

With regard to the $\eta = \theta_{sw}$ model, it weights the side-wall area somewhat too lightly, since it is based on the lowest temperature of the side walls. Therefore, it is believed that the best representation of the Nusselt number lies between those for $\eta = 1$ and $\eta = \theta_{sw}$. Fortunately, these models yield Nusselt numbers which are not very different, so that a reasonable approximation would be to average the Nusselt numbers given by equations (9) and (11) at the Reynolds number of interest.

Attention is now turned to the results of ref. [1] which, as noted earlier, correspond to a smaller interwall spacing than that employed here. In ref. [1], side-wall temperatures were not measured, and the heat transfer coefficient was evaluated using a procedure that corresponds to the present $\eta = 0$ model.

The tabulated results of ref. [1] (available in ref. [2])

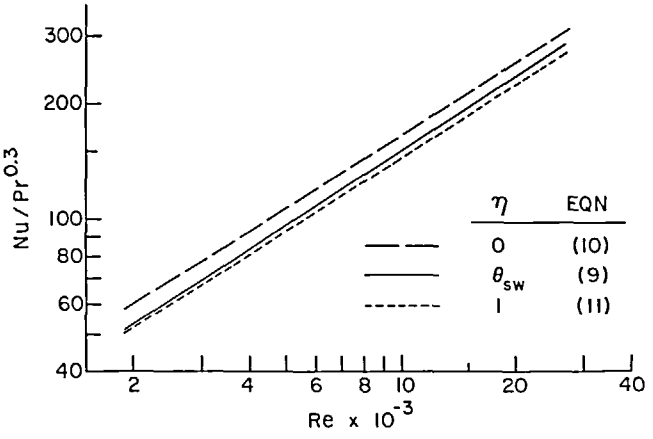

FIG. 6. Comparison of fully developed Nusselt numbers for various weightings of the side-wall area.

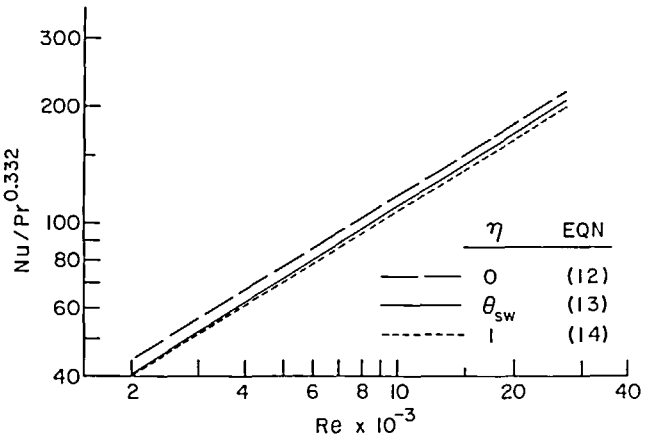

FIG. 7. Fully developed Nusselt numbers of ref. [1] for various weightings of the side-wall area.

were reworked, yielding

$$Nu/Pr^{0.332} = 0.412\,Re^{0.614}, \quad (\eta = 0), \qquad (12)$$

$$= 0.347\,Re^{0.626}, \quad (\eta = \theta_{sw}), \qquad (13)$$

$$= 0.374\,Re^{0.614}, \quad (\eta = 1). \qquad (14)$$

Since θ_{sw} was not measured in [1], equation (8) was employed in the computations which yielded equation (13). Also, the $\eta = 0$ correlation given by equation (12) differs slightly from the correlation given in [1] because a tighter fit of the data was obtained by the procedure used here. In addition, it may be noted that the data of ref. [1] and the fitted equations (12)–(14) correspond to the Prandtl number range from 4 to 8 (as compared to the present range of 4–12).

Equations (12)–(14) have been plotted in Fig. 7, and the corresponding straight lines are ordered with η in the same way as those of Fig. 6. However, the overall spread of the lines, which reflects the range between the upper and lower limits of the side-wall effect, is smaller in Fig. 7. This is because the side walls in ref. [1] are smaller than those of the present configuration ($A_{sw}/A_w = 0.1$ compared with $A_{sw}/A_w = 0.145$). The gap between the $\eta = \theta_{sw}$ and $\eta = 1$ lines in Fig. 7, already small, would have been even smaller had the θ_{sw} values appropriate to the experiments of ref. [1] been available.

A comparison will now be made between the present Nusselt number results and those of ref. [1]. The presented comparison corresponds to the $\eta = \theta_{sw}$ data-reduction model, but the $\eta = 1$ model yields an almost identical comparison. Also, to obtain uniformity of the Prandtl number range, the present data for $4 \leqslant Pr \leqslant 8$ have been used for the comparison. These data are very well correlated by the equation

$$Nu/Pr^{0.332} = 0.385\,Re^{0.643}, \quad (\eta = \theta_{sw}). \qquad (15)$$

The Nusselt number data for the comparison and their correlating lines are shown in Fig. 8. Inspection of the figure indicates that the Nusselt numbers for the present duct configuration lie about 30% above those for the configuration employed in ref. [1]. It thus appears, at least at first thought, that an increase of the interwall spacing improves the heat transfer performance of the corrugated duct. However, such a conclusion has to be viewed with considerable caution.

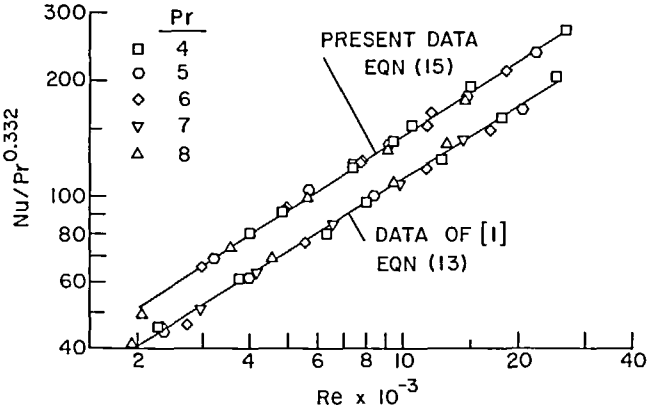

FIG. 8. Comparison of fully developed Nusselt numbers from the present experiments with those of ref. [1] (side-wall weighting: $\eta = \theta_{sw}$).

In particular, the Nusselt number encompasses more than the heat transfer coefficient, and the hydraulic diameter which appears in the Nusselt number is about 39% larger for the present duct configuration than for that of ref [1].

In view of the foregoing, it cannot be concluded that the increase in the Nusselt number necessarily means an increase in the heat transfer coefficient. Rather, to obtain a definitive comparison of the coefficients, the conditions and constraints of the comparison have to be taken into account. Such constrained comparisons will be made in the section on performance evaluations which will follow shortly.

As a final remark about Fig. 8, it can be seen [and confirmed by equations (13) and (15)] that the Reynolds number dependence of the two sets of results is not quite the same. That there is a difference is not unexpected in view of the differences in the pattern of fluid flow revealed by the flow visualization.

Effect of fluid flow inlet conditions

The effect of the fluid flow inlet conditions on the heat transfer characteristics of the corrugated duct is confined to the thermal entrance region. These effects will be presented in terms of the temperature ratio $(T_w - T_b)_x/(T_w - T_b)_{fd}$, which will be plotted as a function of the dimensionless axial coordinate X/D_h.

If the convective heat transfer from the wall to the fluid were independent of axial position, then

$$h_x/h_{fd} = [(T_w - T_b)_x/(T_w - T_b)_{fd}]^{-1}. \qquad (16)$$

Thus, if the temperature ratio exceeds one, $h_x < h_{fd}$, while if the temperature ratio is below one, $h_x > h_{fd}$. The axial uniformity of the convective heat transfer requires that the net axial conduction in the duct wall be negligible. This condition is fulfilled on a per-cycle basis in the thermally developed regime. In the entrance region, for the most part, the measured wall temperatures depart only moderately from the linear distribution, so that the net axial conduction may also be moderate. In view of this and also taking account of the fact that insufficient information is available for determining the net axial conduction, equation (16) will be used in the interpretation of the results.

Representative results for the $(T_w - T_b)$ ratio are presented in Figs. 9–11. Each figure corresponds to a specific Reynolds number (actually, to a narrow range about a nominal value), respectively, 3200, 7300, and 18 700. The data in these figures are for $Pr \simeq 6$, which lies in the mid-range of the investigated Prandtl numbers. Results obtained for other Prandtl numbers show trends identical to those of Figs. 9–11.

Each figure contains three sets of data. The upper set pertains to the unobstructed inlet pictured in Fig. 2(c) [hence the designation case (c)]. The middle and lower sets of data correspond to the presence of a delivery duct which feeds fluid to the inlet. For case (b), the opening of the delivery duct is at the top, while for case (a) the opening is at the bottom. These configurations are respectively pictured in Figs. 2(a) and (b).

From an overall inspection of Figs. 9–11, it is seen that the unobstructed inlet yields the lowest entrance region heat transfer coefficients, the top-open delivery duct yields somewhat higher coefficients, and the bottom-open delivery duct yields the highest coefficients. This trend can be correlated with the degree of turning experienced by the fluid entering the duct. Study of Fig. 2 suggests that case (c) experiences the least turning and case (a) the most turning, with case (b) being intermediate. Therefore, the greater the turning, the higher the entrance region heat transfer coefficients. The disturbance of the flow caused by the turning is believed to be responsible for the increase in the coefficients.

It is interesting to observe from Figs. 9–11 that the entrance region heat transfer coefficients do not differ

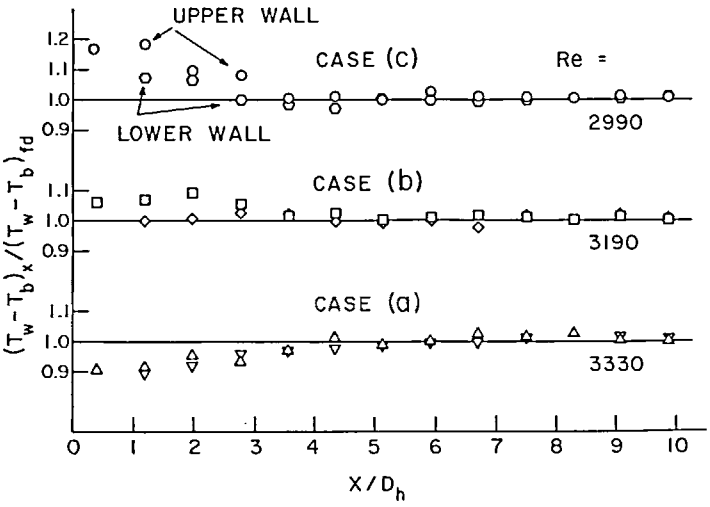

FIG. 9. Axial distribution of the wall-to-bulk temperature difference for various fluid flow inlet conditions, $Re \sim 3200$.

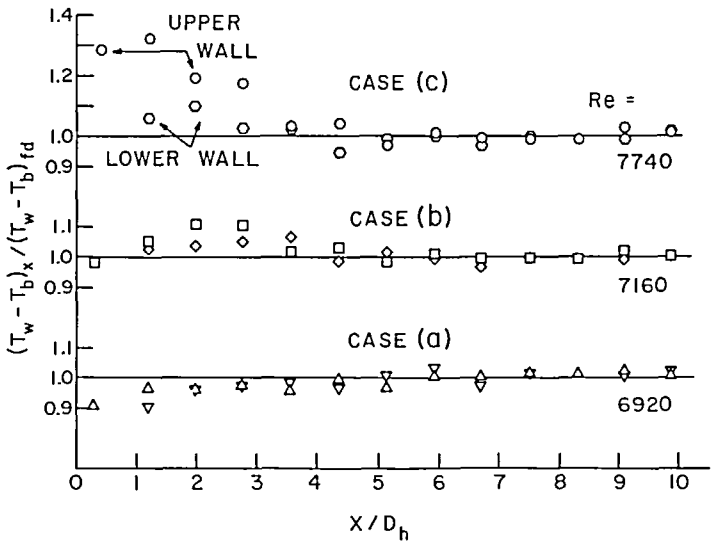

FIG. 10. Axial distribution of the wall-to-bulk temperature difference for various fluid flow inlet conditions, $Re \sim 7300$.

markedly from the fully developed values. Furthermore, it is somewhat surprising, at least at first thought, that the unobstructed inlet [case (c)] yields entrance region coefficients that are lower than fully developed. This is because the flow disturbances created within the corrugated duct are more enhancing than the entrance region phenomena (e.g. thin boundary layers). Even for case (b), the extent of the inlet-adjacent turning is not sufficient to provide enhancement as great as that provided by the in-duct flow disturbances. Only for case (a), which has the greatest inlet-adjacent turning among the investigated cases, are the entrance region coefficients larger than the fully developed value.

The length of the thermal entrance region can be identified by examination of Figs. 9–11. It appears that for virtually all cases, thermal development is complete by $X/D_h = 4$.

FRICTION FACTOR RESULTS

The pressure distribution measurements were aimed at determining fully developed friction factors, so that the fluid flow inlet conditions were not an issue. A typical pressure distribution measurement is shown in Fig. 12, where the normalized pressure difference between ambient and an axial station X is plotted as a function of X'/D_h (X' is a shifted X coordinate). The

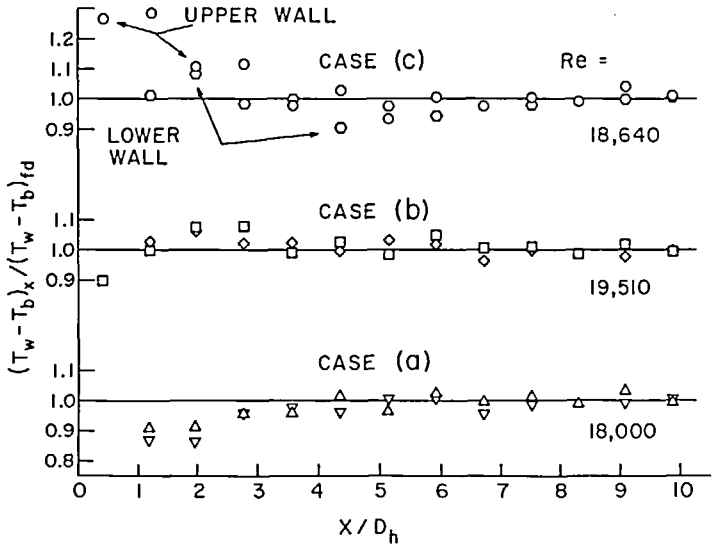

FIG. 11. Axial distribution of the wall-to-bulk temperature difference for various fluid flow inlet conditions, $Re \sim 18700$.

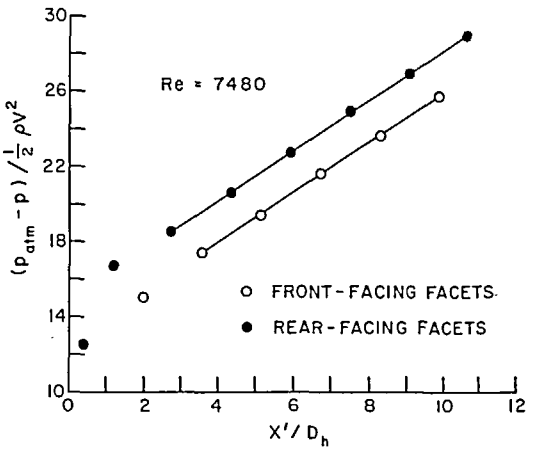

FIG. 12. Representative axial pressure distribution.

open circles correspond to pressures at the mid-points of front-facing facets, while the black circles correspond to the mid-points of the rear-facing facets.

In the fully developed regime, the open circles lie on a straight line, while the closed circles lie on another straight line of identical slope. This behavior is consistent with the characteristics of periodic fully developed flow as discussed in the text preceding equation (7). The slope of the straight lines in Fig. 12 is the friction factor f.

The thus-determined friction factors are listed in Table 1 as a function of the Reynolds number. Two characteristics of the friction factor results are worthy of note. First, the magnitude of f is large, in excess of one. This is very much larger than that for conventional duct flows and exceeds the value 0.57 measured in ref. [1]. Second, the increase of f with Re, although moderate, is uncommon.

These observations prompted supplementary measurements with different instruments to verify the primary set of measurements made with the Baratron

Table 1. Fully developed friction factors

Re	f	Pressure sensor	Flowmeter
1954	1.231	10 Torr Head	9 Scfm Rotameter
1960	1.215	10 Torr Head	9 Scfm Rotameter
2691	1.215	10 Torr Head	9 Scfm Rotameter
3304	1.258	10 Torr Head	9 Scfm Rotameter
4308	1.277	10 Torr Head	9 Scfm Rotameter
5667	1.309	10 Torr Head	Orifice
5690	1.305	10 Torr Head	9 Scfm Rotameter
6015	1.360	10 Torr Head	19 Scfm Rotameter
6017	1.341	100 Torr Head	19 Scfm Rotameter
7476	1.322	100 Torr Head	9 Scfm Rotameter
7919	1.347	100 Torr Head	19 Scfm Rotameter
10450	1.374	100 Torr Head	19 Scfm Rotameter
10870	1.341	100 Torr Head	Orifice
15320	1.377	100 Torr Head	19 Scfm Rotameter
15570	1.386	Manometer	19 Scfm Rotameter
17210	1.380	100 Torr Head	19 Scfm Rotameter
19410	1.354	100 Torr Head	Orifice

pressure sensing heads and the calibrated rotameters. All the supplementary measurements agree well with the primary measurements, lending strong support to the validity of the f values.

The larger f values for the present duct configuration relative to that of ref. [1] may reflect a higher pressure drop penalty caused, for instance, by the enlarged region of flow separation. On the other hand, there may be an uncertainty about the relative size of the pressure drop penalty for the two ducts, since f contains quantities other than the pressure gradient. (A similar uncertainty arose in the interpretation of the Nusselt number change.) This issue will be illuminated by the performance evaluations of the next section.

PERFORMANCE EVALUATIONS

In appraising the performance of the present corrugated duct configuration relative to that of ref. [1], comparisons will be made for three different constraints: (I) identical pumping power PP, (II) identical pressure drop per unit length dp/dX, and (III) identical mass flow $\dot{m}$. The pumping power is equal to the product of the pressure drop and the volume flow, so that $PP \sim \dot{m}(dp/dX)$.

In presenting the results, quantities pertinent to the present configuration will be unsubscripted, while those pertaining to the duct of ref. [1] will be identified with a subscript 1. Also, to obtain a concise set of results, the slight difference in the Reynolds number dependences of equations (13) and (15) will be smoothed by using an average of the two exponents and then refitting the data. This gives

$$Nu/Pr^{0.332} = 0.416\,Re^{0.634}, \quad \text{Present,} \qquad (17)$$

$$Nu/Pr^{0.332} = 0.322\,Re^{0.634}, \quad \text{ref. [1].} \qquad (18)$$

Also, the friction factors will be taken to be constants, $f = 1.28, f_1 = 0.57$.

By ratioing equations (17) and (18) and introducing the duct dimensions, there follows

$$h/h_1 = 0.904(\dot{m}/\dot{m}_1)^{0.634}. \qquad (19)$$

Then, from equation (7) and the aforementioned values of f and f_1,

$$(dp/dX)/(dp/dX)_1 = 0.767(\dot{m}/\dot{m}_1)^2. \qquad (20)$$

Finally, by noting that $PP \sim \dot{m}(dp/dX)$,

$$(PP)/(PP)_1 = 0.767(\dot{m}/\dot{m}_1)^3. \qquad (21)$$

Equations (19)–(21) will now be employed in conjunction with the constraints mentioned earlier in this section to yield

(I) For $PP = (PP)_1$,
$h/h_1 = 0.956$,
$\dot{m}/\dot{m}_1 = 1.093$, $(dp/dX)/(dp/dX)_1 = 0.915$.

(II) For $dp/dX = (dp/dX)_1$,
$h/h_1 = 0.983$,
$\dot{m}/\dot{m}_1 = (PP)/(PP)_1 = 1.14$.

(III) For $\dot{m} = \dot{m}_1$,
$h/h_1 = 0.904$,
$(dp/dX)/(dp/dX)_1 = (PP)/(PP)_1 = 0.767$.

From an examination of the foregoing listing, it is seen that for all the employed constraints, h is slightly less than h_1 (by 2–10%). Thus, the increase in the interwall spacing tends to cause a modest decrease in the heat transfer coefficient. On the other hand, the pressure drop is reduced (or remains the same). On balance, the performance differences between the two ducts are not sufficiently great to indicate a global superiority of one over the other. It appears that the final choice will depend on the specifics of the constraint used in the comparison.

CONCLUDING REMARKS

There were three main foci for the experimental work that has been reported in this paper. The first phase of the work dealt with the effect of increasing the spacing between the corrugated walls on the fully developed heat transfer coefficient and friction factor and on the pattern of fluid flow. For these studies, the results of ref. [1], which correspond to a smaller interwall spacing than that employed here, were used as a basis of comparison. For the evaluation of the fully developed heat transfer coefficient, three models were employed to take account of the noncorrugated side walls which bridge fin-like between the corrugated walls, and the use and evaluation of these models constituted the second phase of the work. The third focus of the work was to determine the effect of the fluid flow inlet conditions on the entrance region heat transfer coefficients.

The increase of the interwall spacing gave rise to a 30% increase in the fully developed Nusselt number relative to that of ref. [1], but the friction factor more than doubled. To assess these findings in greater depth, performance evaluations were carried out for three different constraints: (I) identical pumping power, (II) identical pressure gradient, and (III) identical mass flow. For all these cases, the heat transfer coefficient corresponding to the larger interwall spacing was slightly lower (at most by 10%) than that for the smaller interwall spacing, but the pressure gradient was also lower (or equal). Therefore, the performance differences between the two ducts are not sufficiently great to indicate a clear superiority of one over the other.

The flow visualization studies showed that with an increase in the interwall spacing, more of the duct surface area is blanketed by a recirculating flow which is spawned by separation at the peaks of the corrugation facets.

The side walls of the duct were not externally heated but received heat from the corrugated walls by conductive contact. Side-wall temperatures were measured and were employed to weight the side-wall area in the evaluation of the cycle-average fully developed heat transfer coefficient. Other weights were also employed, and it was found that equal weighting of the side-wall and corrugated-wall areas, while not exact, yielded results of satisfactory accuracy.

Three different fluid flow inlet conditions were investigated. In one, the inlet faced onto a large, open plenum chamber, while in the other two cases the flow was forced to turn as it entered the duct. The turning of the flow served as an enhancement mechanism, so that the greater the turning, the higher the measured entrance region heat transfer coefficients.

The thermal entrance region measurements also indicated that thermally developed conditions were attained within four hydraulic diameters of the inlet.

REFERENCES

1. J. E. O'Brien and E. M. Sparrow, Corrugated-duct heat transfer, pressure drop, and flow visualization, *J. Heat Transfer* **104**, 410–416 (1982).
2. J. E. O'Brien, Corrugated-duct heat transfer, pressure drop, and flow visualization, Ph.D. thesis, Department of Mechanical Engineering, University of Minnesota, Minneapolis, Minnesota (1981).

EFFET DE L'ESPACE ENTRE PAROIS ET DES CONDITIONS D'ENTREE DU FLUIDE SUR UN ECHANGEUR DE CHALEUR A PAROI CORRUGUEE

Résumé—On détermine expérimentalement le transfert thermique, la perte de charge et les configurations de l'écoulement pour de l'eau en écoulement dans un canal à parois corruguées. On considère les effets de l'espace variable entre les parois et de différentes conditions d'entrée du fluide; on examine aussi le rôle de la paroi latérale plane dans l'évaluation du coefficient de transfert. L'augmentation de l'espace entre parois donne lieu à un accroissement sensible du nombre de Nusselt pleinement établi (trente pour cent pour la variation considérée de l'espacement), mais le coefficient de frottement croît de façon plus marquée (plus que d'un facteur deux). Des évaluations de performance sont données pour trois constraintes différentes—puissance de pompage fixée, perte de charge fixée, débit massique fixé. Pour tous ces cas, le coefficient de transfert thermique pour le plus grand espacement est légèrement plus faible que celui pour le plus petit espacement, mais la perte de charge est elle aussi plus faible. Des configurations d'entrée de fluide sont employées qui créent différents degrés de courbure de l'écoulement. On trouve que plus fort est le virage, plus le coefficient de transfert thermique dans la région d'entrée est élevé.

DER EINFLUSS DES WANDABSTANDS UND DER ZUSTRÖMBEDINGUNGEN AUF DAS VERHALTEN EINES WÄRMEÜBERTRAGERS MIT GEWELLTEN WÄNDEN

Zusammenfassung—Bei der Strömung von Wasser durch einen Kanal mit gewellten Wänden wurden Wärmeübergang, Druckabfall und die Strömungsformen bestimmt. Dabei wurde der Einfluß des Abstands zwischen den gewellten Wänden und verschiedener Zuströmbedingungen betrachtet. Der Einfluß der nichtgewellten Seitenwände bei der Bestimmung des Wärmeübergangskoeffizienten wurde berücksichtigt. Eine Zunahme des Wandabstands führte zu einem spürbaren Anwachsen der *Nu*-Zahl (dreißig Prozent im untersuchten Bereich), der Widerstandsbeiwert stieg jedoch stärker an (mehr als das Zweifache). Die Untersuchungen wurden für drei verschiedene Betriebsbedingungen durchgeführt—konstante Pumpenleistung, konstanter Druckabfall und konstanter Massenstrom. In all diesen Fällen war der Wärmeübergangskoeffizient bei größerem Wandabstand etwas geringer als bei kleinerem Abstand, ebenso der Druckabfall. Das Wasser wurde so zugeführt, daß sich unterschiedliche Umlenkungen der Strömung ergaben. Dabei zeigte sich, daß der Wärmeübergangskoeffizient im Eintrittsgebiet bei stärkerer Umlenkung höher ist.

ВЛИЯНИЕ РАССТОЯНИЯ МЕЖДУ СТЕНКАМИ И УСЛОВИЙ ВХОДА ПОТОКА ЖИДКОСТИ НА ХАРАКТЕРИСТИКИ ТЕПЛООБМЕННИКА С ГОФРИРОВАННЫМИ СТЕНКАМИ

Аннотация—Проведено экспериментальное определение теплообмена, перепада давления и картины течения потока жидкости при движении воды в канале с гофрированными стенками. Особое внимание обращено на влияние изменения расстояния между гофрированными стенками при различных условиях входа потока жидкости, а также негофрированных боковых стенок на коэффициент теплопереноса. С увеличением расстояния между стенками значение полностью развитого числа Нуссельта существенно увеличивалось (на 30% при исследуемом изменении расстояния), однако в большей степени возрастал коэффициент трения (более чем в два раза). Проведены оценки характеристик теплообменника при трех различных допущениях: фиксированная мощность насоса, фиксированный перепад давления и фиксированный поток жидкости. Во всех этих случаях коэффициент теплопереноса при большем расстоянии между стенками был несколько ниже значения, полученного при меньшем расстоянии, но также ниже был и перепад давления. Изучалось влияние условий входа жидкости, которые создавали различные степени поворота потока. Найдено, что при большем повороте потока получаются более высокие коэффициенты теплопереноса в области входа.